JOURNAL OF MATERIALS SCIENCE **33** (1998) 5001–5006

Combustion synthesis, powder characteristics and crystal structure of phases in Ce–Pr–O system

M. RAJENDRAN, K. K. MALLICK, A. K. BHATTACHARYA*
Centre for Catalytic Systems and Materials Engineering, Department of Engineering, University of Warwick, Coventry CV4 7AL, UK
E-mail: m.g.rajendran@warwick.ac.uk

The combustion method has been employed to produce homogeneous, single phased mixed rare-earth oxides in $Ce_{1-x}Pr_xO_{2-y}$ system for x ranging from 0 to 0.7. A cubic fluorite structure is formed for the compositions $0 \leq x \leq 0.7$, while for $x > 0.7$ mixed phases are obtained. The mixed oxides are formed at the furnace temperature of 500 °C in a short duration of 10 min. In view of the importance of these powders in catalysis, crystallite size, surface area and porosity measurements have been carried out. The crystallite size of the powders increases with x while the surface area decreases. As the temperature is increased to 850 °C, the surface area decreases and the effect is much pronounced in cerium rich oxides. The powders on calcination above 900 °C in air results in the demixing of Ce and Pr to give two fluorite phases.

1. Introduction

Ceria-based materials are used extensively as catalysts, oxygen sensors and as a component in electroceramic formulations [1, 2]. These applications have prompted a thorough investigation on the basic issues concerning the composition, structure and their influence upon the evolution of properties. CeO_2 is an important constituent in three-way catalyst formulations for treating the automotive exhaust as it provides surface active sites for the reaction and also acts as an oxygen storage/transport/release medium. The ability of ceria to store/release oxygen is primarily caused by the fluorite crystal structure that it adopts and the mixed valence of cerium, Ce^{3+}/Ce^{4+}. The fluorite lattice having a metal ion of variable valency is flexible to release oxygen to accommodate significant amount of oxygen vacancies under reducing conditions. These vacancies will be refilled with oxygen atoms under oxidizing conditions. This reversible oxygen storage/release feature coupled with chemical stability in adverse conditions is a unique feature that offers ceria the prime position in three-way catalyst design. Other important features are that ceria promotes the water-gas shift reaction [3–5], and it stabilizes the dispersion of noble metals on metal oxide supports [6].

The process of oxygen storage and transport in ceria occurs through the lattice oxygen defects. These defects could be either intrinsic or extrinsic depending on the mode of creation of the oxygen vacancies [7]. These oxygen defects play an important role in promoting the catalytic activity of ceria-based materials. Metal ions such as Zr [8, 9], Tb [10], Gd [7], Pb [11], and Pr [12] in CeO_2 have been found to create oxygen vacancies and improve the catalytic activity and redox properties to a considerable extent. The enhancement in the activity is attributed to high oxygen ion mobility in the fluorite lattice. In few cases, the mixed oxides enable O_2 diffusion at relatively lower temperatures and improve the catalyst efficiency [13] which is of immense practical significance. There are a few mixed oxides based on ceria showing improved thermal [14], redox [14, 15] and catalytic properties [13, 16] and the compositions in Ce–Pr–O system are more promising than the trivalent rare-earth substituted ceria formulations because of the mixed valence of praseodymium.

The crystal structure and defect chemistry of cerium and praseodymium oxides are interesting and they modulate the properties of these oxides. The oxygen non-stoichiometry in ceria is limited compared to Pr–O system. Praseodymium forms a wide range of non-stoichiometric oxide phases and also an homologous series of oxides with the generic formula Pr_nO_{2n-2}, with $n = 4, 7, 9, 10, 11, 12$ and ∞. The structure of these oxides may be viewed as formed by removal of oxygen atoms from normal sites in the fluorite structure accompanied by a relaxation of the remaining atoms proportionate to the extent of oxygen vacancy. Although Pr_nO_{2n-2} and CeO_2 crystallize in fluorite structure, the solid solubility of Pr in CeO_2 is restricted to only about 70 mol %. There exists only a few reports on the Ce–Pr–O system [17, 18].

Synthesis of mixed metal oxides by non-conventional methods offers the advantage of achieving phase purity and chemical homogeneity [19–25]. The resultant oxides possess fine particle size and large surface area. Among various methods, the combustion process is attractive since it requires only a short duration of few minutes to produce the metal oxides [26–28]. In

* Corresponding author.

the present paper we report the combustion synthesis of mixed metal oxides in $Ce_{1-x}Pr_xO_{2-y}$ system for $0 \leq x \leq 1.0$. The oxides have been characterized for solid solubility and unit cell parameters. The powder characteristics such as crystallite size, surface area and porosity have been determined as a function of x. The variation of surface area and porosity as a function of calcination temperature has also been studied.

2. Experimental Details

2.1. Materials

2.1.1. Preparation of $Ce_{1-x}Pr_xO_{2-y}$ fine powders

All chemicals and reagents used were of high purity and commercially available (Aldrich) $(NH_4)_2Ce(NO_3)_6$ (99.99%), $Pr(NO_3)_3.6H_2O$ (99.9%) and urea (99%) were used as received. The required quantities of metal nitrates were mixed together to desired stoichiometry and urea was added following the oxidizer/fuel (O/F) ratio as detailed elsewhere [26–28]. The metal nitrate–urea mixture was dissolved in minimum amount of water and the contents transferred to a large volume glass evaporating dish. The dish was introduced in a pre-heated muffle furnace maintained at 500 °C inside a fume-hood. In a few minutes water evaporated and the contents underwent frothing and ignited to give a voluminous oxide powder.

2.2. Characterization

2.2.1. X-ray powder diffraction (XRD) measurement

X-ray powder diffraction patterns for samples treated at various temperatures were recorded in the region of $2\theta = 10$–90° with a step scan of 0.1°/min on a Philips diffractometer (Model PW1830) using CuK_α radiation. Cell parameters were calculated and further refined using linear regression procedures (Philips APD 1700 software) applied to the measured peak positions of all major reflections up to $2\theta = 90^\circ$.

2.2.2. Crystallite size measurements

Crystallite sizes were calculated from the full width at half maximum (FWHM) of the (1 1 1) reflection using Scherrer equation [29]

$$D = k\lambda/\beta_{1/2}\cos\theta \tag{1}$$

where D is the crystallite size, k is a shape function (a value of 0.9 is used), λ is the wave length of the X-ray ($\lambda = 0.1542$ nm, CuK_α radiation) and θ is the angle of incidence. $\beta_{1/2}$ was determined from the experimental integral peak width (FWHM) by applying standard correction for the instrumental broadening.

2.2.3. Surface area and porosity measurements

Specific surface area and pore size distribution measurements were performed on a micromeritics, accelerated surface area and porosimetry system (ASAP 2000). The samples were degassed at 300 °C for 6 h prior to the measurement. The measurement is based on the Brunauer–Emmett–Teller (BET) principle [30]. The BET equation may be written as

$$(P/P_s)/[V(1-(P/P_s))] = (1/V_mC) + [(C-1)/V_mC](P/P_s) \tag{2}$$

where V is the volume of gas adsorbed at pressure P, P_s is the saturation pressure, i.e. the vapour pressure of liquid gas at the adsorbing temperature, V_m is the volume of gas required to form the monolayer and C is a constant related to the energy of adsorption. A plot of $P/V(P_s - P)$ against P/P_s gives a straight line with an intercept and slope of $1/V_mC$ and $(C-1)/V_mC$, respectively. The value of V_m is extracted from a series of measurements made by varying the pressure of adsorbate, N_2.

In order to evaluate the type of pore and pore volume distribution, adsorption–desorption isotherms for the mixed oxides were determined [31]. In a typical experiment, volume of N_2 adsorbed in $cm^3\,g^{-1}$ at STP is monitored against relative pressure (P/P_s), ranging from 0 to 1. The relative pressure was reversed from 1 to 0 to find out the volume of gas desorbed. A plot of volume adsorbed and desorbed against relative pressure gives an isotherm with a characteristic hysteresis from which the type of pore and pore size distribution were determined.

3. Results and Discussion

The XRD patterns of a few selected compositions in the Ce–Pr–O system are given in Fig. 1. Starting with cerium dioxide, as cerium is replaced by praseodymium, single phase compounds of general formula $Ce_{1-x}Pr_xO_{2-y}$ are obtained in the compositional range $0 < x < 0.7$. Beyond $x > 0.7$ mixed phases are obtained. The compositions in $Ce_{1-x}Pr_xO_{2-y}$ crystallize in cubic fluorite structure for $0 < x < 0.7$. All XRD reflections could be indexed on the basis of a cubic

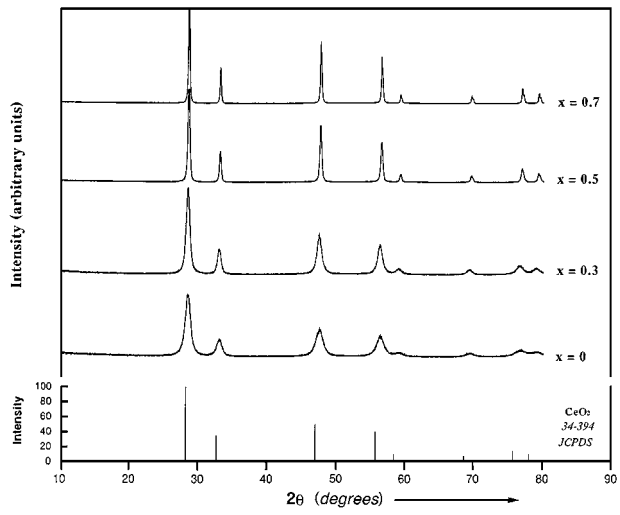

Figure 1 Powder XRD patterns of selected compositions in $Ce_{1-x}Pr_xO_{2-y}$ system.

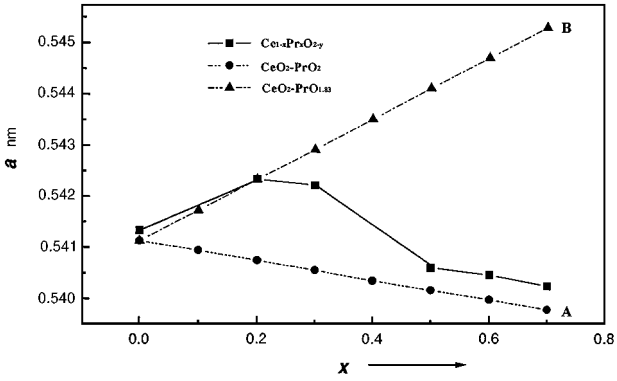

Figure 2 Variation of cell parameter, a with x for $Ce_{1-x}Pr_xO_{2-y}$; (A) calculated by using Vegard's law for solid solutions between the dioxides of cerium and praseodymium and (B) for CeO_2–$PrO_{1.83}$. Experimental results of the present study in solid line.

fluorite unit cell. The refined cell parameter, a is plotted against x in Fig. 2. For $x = 0$ to 0.3, the value of a shows a slight increase. The cell parameter a decreases as x is increased above 0.3. As the ionic radii of Ce^{4+} and Pr^{4+} in eightfold co-ordination are 0.097 and 0.096 nm, respectively, only minor variations are observed in this compositional range. The dotted line in Fig. 2 is based on Vegard's rule and gives a theoretical estimate of a as a function of x. The following expression gives a linear relation between a and x, where Pr^{4+} substitutes for Ce^{4+} in the lattice sites

$$a_x = -0.0193x + 0.5411 \text{ nm} \quad (3)$$

This relationship is arrived at from the reported cell parameters of the dioxides of cerium and praseodymium [JCPDS file: 34-394 and 24-1006]. The solid solution formation between the dioxides is inferred for $x > 0.3$ because the variation of a parameter with x is showing a decreasing trend. Loss of oxygen from the fluorite lattice can result in the creation of oxygen vacancies. This process can result in the reduction of proportionate amount of tetravalent metal ions to the trivalent state to maintain charge neutrality. The trivalent ions are larger in size ($Pr^{3+} = 0.1126$ nm and $Ce^{3+} = 0.1143$ nm in eightfold co-ordination) compared to the tetravalent ions and hence a significant increase in the cell parameter is expected corresponding to the amount of trivalent ions present in the lattice. This is often the case when the oxides are prepared at elevated temperatures. On the other hand, chemical methods of synthesis gives rise to oxides having fewer oxygen vacancies since the oxides are formed at lower temperatures. The present results show the solid solution formation between CeO_2–$PrO_{1.83}$ for $x < 0.3$, since the a parameter increases with x. The dotted line in Fig. 2 is based on Vegard's rule for the formation of solid solution between CeO_2 and $PrO_{1.83}$. The variation of cell parameter with x for CeO_2–$PrO_{1.83}$ system can be as given below following Vegard's rule

$$a_x = 0.058x + 0.5411 \text{ nm} \quad (4)$$

These variations in cell parameters are caused by the lattice oxygen vacancies. The variations in oxygen stoichiometry are brought about by the nature of the combustion process which depends on the proportion of metal ions in the mixture. The redox mixtures rich in ceric ammonium nitrate are likely to raise the flame temperature causing the creation of oxygen vacancies. An increase in the amount of praseodymium nitrate in the redox mixture is expected to lower the flame temperature to minimize the loss of lattice oxygen in the resultant solid solution. As the nature of the oxidizer, fuel and the oxidizer to fuel (O/F) ratio decide the energetics of the combustion process, it is important to fix these parameters. In the present case, this is fixed by using metal nitrates as the oxidizer and urea as the fuel and the optimum O/F ratio has been employed as it has previously been used for other systems [26–28]. It is to be noted that only an optimum O/F ratio results in the ignition and self-propagation of the combustion reaction to produce the mixed oxides. This process is autocatalytic and requires only a thermal initiation at a temperature of 500 °C. Once initiated, the combustion reaction proceeds with intense flame and is complete within about 30 s. The fine solid mass left behind is the mixed oxide which can be heated at 500 °C for further 5 min to drive away the adsorbed and trapped gases.

These aspects reveal the fact that the synthesis conditions influence the oxygen stoichiometry and eventually the unit cell parameter of these compositions. As the praseodymium–oxygen system is known to form a wide range of non-stoichiometric oxide phases, the mixed oxides containing Pr in the lattice are expected to show this behaviour to a considerable extent depending on the type of crystal structure that they adopt. The fluorite, perovskite and pyrochlore structures are known to accommodate considerable lattice oxygen vacancies.

Fig. 3 shows the variation of crystallite size as a function of x for the oxides obtained at 500 °C. As can be seen the crystallite size decreases as the Pr-content is increased in $Ce_{1-x}Pr_xO_{2-y}$. The dependence of crystallite size upon composition in ceria-based oxides have considerable practical importance, since this could bring about changes in the physical properties. The free energy of a spherical Ce–Pr–O microcrystal may be expressed as [32]

$$G = (4/3)\pi r^3 \psi + 4\pi r^2 \sigma \quad (5)$$

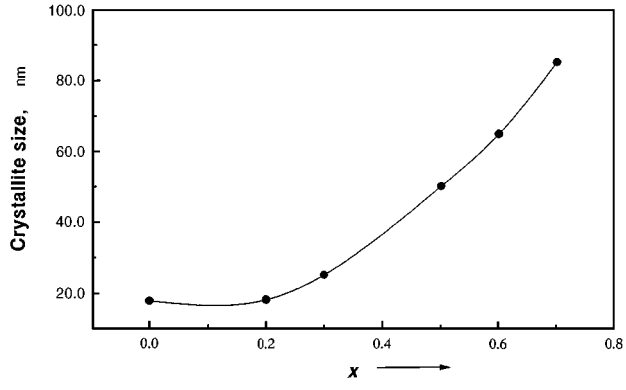

Figure 3 Variation of crystallite size (D) with x in $Ce_{1-x}Pr_xO_{2-y}$ system.

where r is the radius of the crystallite, ψ is the free energy/unit volume of a large crystal and σ is the surface free energy of the crystallite. Thus, the smaller crystallites possess large surface free energy to influence the physicochemical properties.

Smaller crystallites are known to possess excess energy associated with their surface as given below [33]

$$\Delta E = [12N(n-1)^2 d^2 K\gamma]/n^3 \qquad (6)$$

where ΔE is the excess energy in kcal mol^{-1}, N is Avogadro's number, d is the diameter of the oxygen ion, K is a factor to convert the energy unit from ergs to kilocalories, n is number of ions per cube edge in the fluorite structure, d is the diameter of the oxygen ion and γ is the surface energy in ergs cm^{-2}. Crystallites in the size range below 10 nm possess over sixfold excess surface energy than the large crystallites of about 100 nm in size. The mixed oxides in the present case for $x < 0.3$ have crystallite size falling in the sizes range 17–25 nm and determined from the above relation to have about three fold excess energy. The surface energy comes down as the crystallite size goes up and for the limiting composition in the series ($x = 0.7$) it is almost the same as that of the bulk material. These compositions having large crystallites are calculated not to show any behaviour which might originate from excess energy. This relation can be used as a simple predictive guide to identify whether a sample posses excess energy associated with its active surface. Interestingly, by knowing the crystallite size, the magnitude of excess energy can be calculated. This relation is experimentally found to be valid for oxides especially for the fluorites [24]. Thus, in $Ce_{1-x}Pr_xO_{2-y}$ system, the Pr-content influences the excess energy associated with the powders by varying the crystallite size. When heated to higher temperatures the crystallites grow and the specific surface area and the excess surface energy diminsh. The extent of reduction in surface area against x is given in Fig. 4. The samples obtained at two selected temperatures of 500 °C and 850 °C are given. The drastic decrease in the surface area of the cerium rich samples, for example $x = 0$ is a consequence of the excess surface energy driving the crystallite growth.

The specific surface areas of the mixed oxides obtained at 500 °C show a decreasing trend as the Pr-content is increased in $Ce_{1-x}Pr_xO_{2-y}$ (Fig. 4). For example, CeO_2 has the largest surface area of 78.6 m^2 g^{-1} in this series and it decreases to 65.2 m^2 g^{-1} for $x = 0.2$

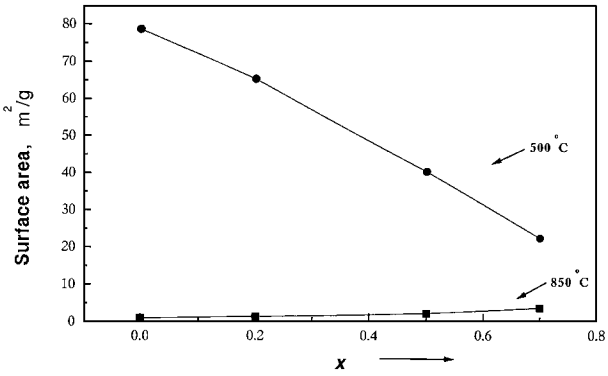

Figure 4 Variation of surface area with x in $Ce_{1-x}Pr_xO_{2-y}$ for calcination at two temperatures, (a) 500 °C and (b) 850 °C.

and decreases further to 22.3 m^2 g^{-1} for $x = 0.7$. The decreasing trend in specific surface area as a function of x is consistent with the XRD results on the crystallite size measurements. An increase in the calcination temperature to 850 °C brings about significant reduction in the surface area of the cerium rich compositions. On the other hand, the limiting composition $x = 0.7$ shows relatively small decrease in surface area. Table I gives the surface area of the compositions in the series.

Adsorption–desorption isotherms were obtained for few compositions to find out the type of pores and the pore size distribution (Fig. 5). Below the critical temperature of the adsorbate, the presence of pores give rise to capillary condensation and is observed as a hysteresis in the adsorption–desorption isotherm. The isotherms of the oxides show narrow hysteresis revealing the presence of cylindrical pores in the samples. As it is seen from Fig. 5, the desorption branch lies close to the adsorption branch to give hysteresis when the relative pressure is above 0.8 for $x = 0$ and it is found to be 0.45 for $x = 0.7$. The shape of the hysteresis suggests the presence of cylindrical pores and their diameter increasing with x. It is interesting to note that the average pore diameter increases as the Pr-content is increased. The composition $x = 0.7$ shows the largest hysteresis among the other members in the series. As the Pr-content increases the hysteresis becomes wider and there is a profound increase in the magnitude of volume adsorbed as a function of relative pressure as shown in Fig. 5. The base composition, CeO_2 ($x = 0$) adsorbs 17.93 cm^3 g^{-1} of nitrogen at a relative pressure of 0.06 whilst the limiting composition ($x = 0.7$) adsorbs only 4.89 cm^3 g^{-1}. However, when the relative

TABLE I Summary of XRD and surface area measurements for Ce_{1-x}–Pr_xO_{2-y} system

			Surface area (m^2 g^{-1})	
x	Lattice parameter (nm)	Cell volume (nm^3)	500 °C	850 °C
0	0.5413(4)	0.15865	78.6	0.9
0.2	0.5423(3)	0.15962	65.2	1.3
0.3	0.5422(1)	0.15950	–	–
0.5	0.5406(0)	0.15799	54.5	2.0
0.6	0.5404(5)	0.15787	–	–
0.7	0.5402(4)	0.15767	22.3	3.6

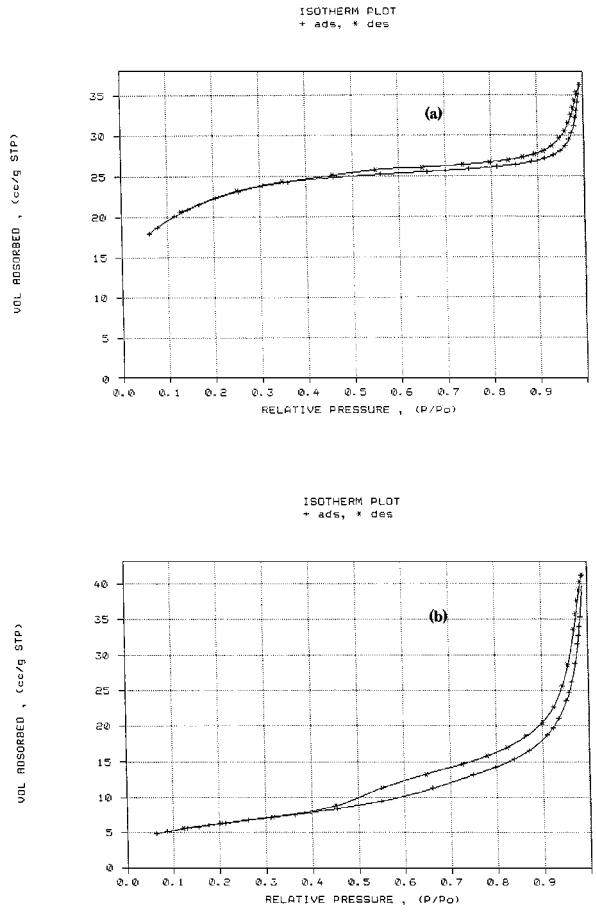

Figure 5 Adsorption–desorption isotherms of samples prepared at 500 °C: (a) $x = 0$ and (b) $x = 0.7$ in $Ce_{1-x}Pr_xO_{2-y}$ system.

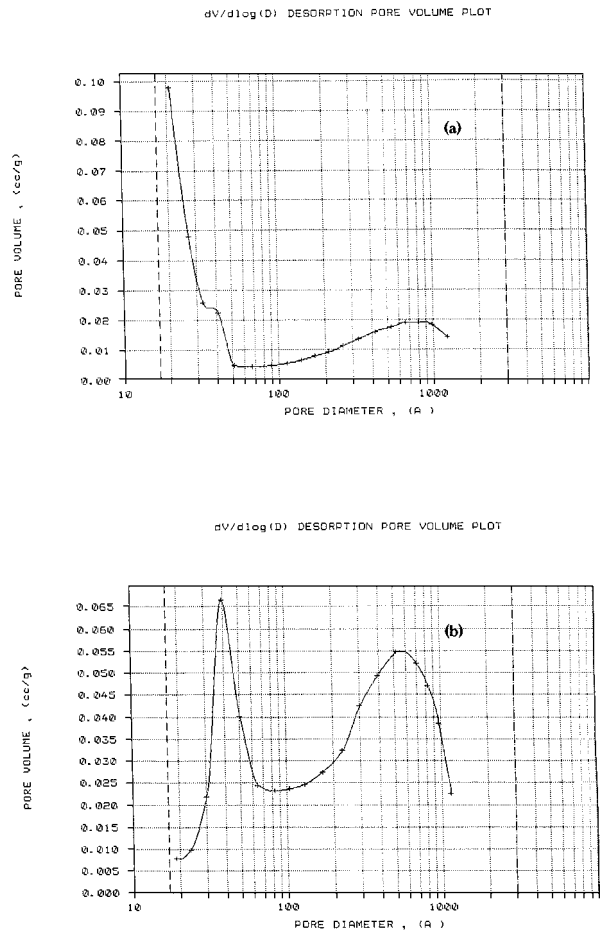

Figure 6 Pore size distribution of samples prepared at 500 °C: (a) $x = 0$ and (b) $x = 0.7$ in $Ce_{1-x}Pr_xO_{2-y}$ system.

pressure is increased to about 0.98, the amount of gas adsorbed by $x = 0.7$ and $x = 0$ are 42 and 37 $cm^3\ g^{-1}$, respectively. Although there is a decrease in BET surface area as Pr-content is increased, the adsorption–desorption isotherms reveal an increased porosity in the mixed oxides. This is clearly seen from the plot of pore volume against pore diameter for $x = 0$ and 0.7 as shown in Fig. 6. The distribution of pore diameter for two selected compositions, $x = 0$ and $x = 0.7$ are shown in Fig. 6. The $x = 0$ composition gives only a single broad feature, whereas $x = 0.7$ gives two intense features, the first one narrow and the second one relatively broad. This result suggests that Pr-content brings about significant changes in the porosity characteristics of these mixed oxides. The average pore diameter determined from the desorption results for $x = 0$ and $x = 0.7$ are 4.08 and 9.88 nm, respectively.

4. Conclusions

The combustion method has been employed to produce $Ce_{1-x}Pr_xO_{2-y}$ fine powders in a short duration of 10 min at a furnace temperature of 500 °C. The solid solubility of Pr extends up to $x = 0.7$ in $Ce_{1-x}Pr_xO_{2-y}$. The crystallite size of cerium-rich compositions are found to be larger and it decreases as x is increased in $Ce_{1-x}Pr_xO_{2-y}$. The surface area measurements on the solid solutions show a strong dependence on x and it decreases as x is increased. At higher temperatures, cerium rich compositions show a pronounced decrease in surface area while the porosity increases as a function of x. The present study reveals the compositional dependence of powder characteristics in mixed rare-earth oxides.

Acknowledgement

The authors would like to thank the EPSRC and the Centre for Catalytic Systems and Materials Engineering for providing fellowships to M.R. and K.K.M., respectively.

References

1. K. C. TAYLOR in "Catalysis, science and technology," edited by J. R. Anderson and M. Boudart (Springer Verlag, Berlin, 1984) p. 119.
2. M. YOSHIMURA, *Amer. Ceram. Soc. Bull.* **67** (1988) 1950.
3. H. S. GANDHI, A. G. PIKEN, M. SHELEF and R. G. DELOSH, SAE Paper 760201, 1976.
4. J. C. SCHLATTER and P. J. MITCHELL, *J. Ind. Eng. Chem. Prod. Res. Dev.* **19** (1980) 288.
5. R. K. HERTZ and J. A. SELL, *J. Catal.* **94** (1985) 166.
6. B. HARRISON, A. F. DIWELL and C. HALLETT, *Platinum Metals Rev.* **32** (1988) 73.
7. B. K. CHO, *J. Catal.* **131** (1991) 74.
8. P. FORNASIERO, R. DI MONTE, G. R. RAO, J. KASPAR, S. MERIANI, A. TROVARELLI and M. GRAZIANI, *ibid.* **151** (1995) 168.
9. T. MUROTA, T. HASEGAVA, S. AOZASA, H. MATSUI and M. MOTOYAMA, *J. Alloys and Comp.* **193** (1993) 298.
10. F. ZAMAR, A. TROVARELLI, C. DE LEITENBERG and G. DOLCETTI, *Stud. Surf. Sci. Catal.* **101** (1996) 1283.

11. Y. ZHANG, A. ANDERSON and M. MUHAMMED, *Appl. Catal. B: Environ.* **6** (1995) 325.
12. A. D. LOGAN and M. SHELEF, *J. Mater. Res.* **9** (1994) 468.
13. F. ZAMAR, A. TROVARELLI, C. DE LEITENBURG and G. DOLCETTI, *J. Chem. Soc. Chem. Commun.* **9** (1995) 965.
14. M. PIJOLAT, M. PRIN, M. SOUSTELLE, O. TOURET and P. NORTIER, *J. Chem. Soc. Faraday Trans.* **91** (1995) 3941.
15. P. FORNASIERO, G. BALDUCCI, R. DI MONTE, J. KASPAR, V. SERGO, G. GUBITOSA, A. FERRERO and M. GRAZIANI, *J. Catal.* **164** (1996) 173.
16. C. DE LEITENBURG, A. TROVARELLI, J. LLORCA, G. BINI and F. CAVANI, *Appl. Catal. A: Gen.* **139** (1996) 161.
17. Y. TAKASU, T. SUGINO and Y. MATSUDA, *J. Appl. Electrochem.* **14** (1984) 79.
18. J. R. MCBRIDE, K. C. HASS, B. D. POINDEXTER and W. H. WEBER, *J. Appl. Phys.* **76** (1994) 2435.
19. D. W. JOHNSON JR, *Amer. Ceram. Soc. Bull.* **60** (1981) 221.
20. L. M. SHEPPARD, *ibid.* **68** (1989) 979.
21. P. PHULE and S. H. RISBUD, *J. Mater. Sci.* **25** (1990) 1169.
22. G. CHO, P. F. JOHNSON and R. A. CONDRATE, *ibid.* **25** (1990) 4738.
23. C. J. BRINKER, G. W. SCHERER in "Sol–gel science" (Academic Press, New York, 1989).
24. L. L. HENCH, D. R. ULRICH (eds), "Science of ceramic chemical processing," (Wiley, New York, 1986).
25. M. RAJENDRAN and M. SUBBA RAO, *J. Solid State Chem.* **113** (1994) 239.
26. J. J. KINGSLEY and L. R. PEDERSON, *Mater. Lett.* **18** (1993) 89.
27. J. J. KINGSLEY, K. SURESH and K. C. PATIL, *J. Mater. Sci.* **25** (1990) 1305.
28. M. M. A. SEKAR, S. S. MANOHARAN and K. C. PATIL, *J. Mater. Sci. Lett.* **9** (1990) 1205.
29. B. D. CULLITY in "Elements of X-ray diffraction" (Addison-Wesley, Reading, MA, 1978) p. 101.
30. S. BRUNAUER, P. H. EMMETT and E. TELLER, *J. Amer. Chem. Soc.* **60** (1938) 309.
31. R. C. GARVIE, *J. Phys. Chem.* **82** (1978) 218.
32. *Idem., ibid.* **69** (1965) 1238.

Received 6 September 1997
and accepted 21 July 1998